Dynamical mechanism for the formation of metastable phases: The case of two nonconserved order parameters

Laurette S. Tuckerman
Department of Mathematics and Center for Nonlinear Dynamics, University of Texas, Austin, Texas 78712

John Bechhoefer
Department of Physics, Simon Fraser University, Burnaby, British Columbia, Canada V5A 1S6

(Received 19 May 1992)

Rapid temperature quenches have long been known to produce metastable thermodynamic phases. We analyze a Landau-Ginzburg model of front propagation and show that metastable phases can arise via a transition that splits the front separating the disordered from the stable phase into one front between the disordered and the metastable phases and another between the metastable and the stable phases. For systems described by a single nonconserved order parameter, the splitting transition is continuous with no hysteresis as the control parameter is varied. For two order parameters, the transition can be continuous, hysteretic, or require a finite-amplitude perturbation. We also discuss briefly applications to pattern-forming systems, where the pattern formed behind a propagating front may change discontinuously as the front velocity is increased.

PACS number(s): 64.60.My

I. INTRODUCTION

Metastable phases of matter are commonplace in nature. At ambient temperatures and pressures, for example, two forms of carbon are found, graphite and diamond, although diamond has a higher free energy than graphite [1,2]. Other elements with coexisting "allotropes" include tin and manganese [3]. If we turn our attention to alloys and mixtures, the number of known metastable phases is almost limitless. Indeed, it has been claimed that "almost no metallic material of importance to a materials scientist is thermodynamically stable" [4]. Much of the interest of the materials scientist arises from the unusual physical properties possessed by many metastable materials. For example, diamond, in addition to being the hardest material, also has the highest room-temperature thermal conductivity. As another example, the hardest form of common steel, martensite, is metastable and is formed by cooling austenite steel at rates of about 200 °C/sec [5].

Experimentally, metastable phases can be created by rapidly cooling or quenching a liquid. Indeed, the development, in the early 1960s, of techniques such as "splat cooling" at rates of 10^6–10^8 °C/sec led to the discovery of vast numbers of metastable phases [6]. Explanations for the formation of metastable phases have focused on two mechanisms [7]: In the first, the *nucleation* rate of metastable germs exceeds that of stable germs. Even though the bulk driving force is always larger for the stable phase, either a low solid-liquid surface tension or the presence of catalytic sites on the sample container can favor the metastable phase. In the second mechanism, the *growth* rate of the metastable phase exceeds that of the stable phase. Such a situation can occur, for example, if the stable phase has a faceted solid-liquid interface while the metastable phase has a molecularly rough interface [8]. Even if the two solid phases nucleate in comparable proportions, the bulk will be largely metastable if the metastable phase grows more rapidly than the stable one does. Both these mechanisms imply that a small amount of the stable phase will be created along with the metastable one, so that eventually the stable phase will grow throughout the sample. If the temperature is rapidly reduced, however, the kinetics may become so sluggish that neither phase grows and the proportion of stable to metastable phases becomes frozen in at a high-temperature value. A third way to form metastable phases is by going to a region where one phase is stable, nucleating it, and then going to a different part of the phase diagram where the created phase is now metastable. If the barrier to nucleating the stable phase is very high, for example, the system will stay in the metastable phase. This is the basis for one method of growing diamonds artificially [1].

In a previous Letter, written in collaboration with Löwen, we proposed a fourth mechanism for the formation of metastable phases during quenching [9]. Our mechanism identifies an instability of the moving interface between the stable solid and the liquid phase. Specifically, we show that for large undercoolings and high velocities, the interface can split into two fronts. The leading front separates the liquid from the metastable phase, the trailing front the metastable from the stable solid. When the leading front moves faster than the trailing front, an arbitrarily large amount of metastable phase may be created. Two questions arise: Under what conditions will the liquid-metastable front move faster than the metastable-stable front? And second, given the required condition on front velocities, will plausible initial conditions lead inevitably to front splitting? Both conditions must be fulfilled in order for the front to split.

A unique feature of our mechanism is that direct nu-

cleation of the metastable phase is not required. Rather, the metastable phase "wets" the surface dividing the stable solid from the liquid. Indeed, the transition is nothing more than the nonequilibrium generalization of the much-studied surface melting [10,11] and wetting transitions [12–14] that occur in thermodynamic equilibrium. In the nonequilibrium version of the wetting transition, a phase that never wets the interface in equilibrium may do so when the interface moves sufficiently fast. The front-splitting transition also resembles models of kinetic disordering of solids [15,16], where a rapidly moving solid-liquid interface leads to a disordered solid. In our case, we consider the formation of ordered metastable phases, which leads to a number of differences with respect to the kinetic-disordering models. Our mechanism is similar to one that has been studied in the context of reaction-diffusion equations [17] and also of propagating patterns in nonlinear systems [18,19].

In our Letter, we discussed the splitting transition in the case of a system modeled by a single nonconserved order parameter [9]. In that case, we found that the splitting transition was always continuous. That is, the front between the stable and liquid phases begins to separate only when a critical undercooling is exceeded. The initial splitting velocity is arbitrarily small, and there is no hysteresis as the system is cycled above and below the critical undercooling.

In this article, we generalize to the case of two nonconserved order parameters. (Prior discussions of the consequences of multiple order parameters—whether for thermodynamic or pattern-forming systems—have concentrated on systems in or near equilibrium [20–24].) For two order parameters, we show that the splitting transition can be hysteretic or finite amplitude. When the transition is hysteretic, the splitting appears at finite separation velocity as the undercooling is varied. When the transition is finite amplitude, the perturbation required to split a front between the disordered and stable phases might be so large that splitting will in practice not be seen. We shall argue in the discussion that the two-order-parameter case is more general than it appears, essentially because the three phases define a plane in order-parameter space.

In Sec. II, we define our model of solidification. In Sec. III, we review the results of the one-order-parameter case. In Sec. IV, we show how, with two order parameters, there are other scenarios for the splitting transition. In Sec. V, we argue that we usually need consider no more than two nonconserved order parameters, and also that one generally expects a splitting transition to occur for large undercoolings. We conclude with a discussion of pattern-formation and phase transition experiments where one might be able to observe the splitting transition. Numerical methods are detailed in an appendix.

II. LANDAU-GINZBURG MODEL FOR FRONT MOTION

We shall consider systems with one spatial dimension, described by a coordinate x ranging over $(-\infty,+\infty)$. We model the solid-liquid transition via a set of coupled Landau-Ginzburg equations for two nonconserved order parameters $a(x,t)$ and $p(x,t)$. As usual, the free energy is the sum of two terms: one a function of the local values of the order parameters, the other a function of their gradients. Since we shall be considering the consequences of three locally stable phases, we take the local free energy per unit volume F to be the sum of three Gaussians. Our results are qualitatively independent of the detailed shape of the potential, so that the precise form of F will be unimportant. With all the Gaussian widths set to $a=\sqrt{0.3}$, $F(q,p)$ is given by

$$F(q,p)=-\sum_{j=0}^{2} h_j e^{-[(q-\hat{q}_j)^2+(p-\hat{p}_j)^2]/a^2} . \tag{1}$$

Although the centers of the three individual Gaussian wells $j=0,1,2$ are located at $(\hat{q}_j,\hat{p}_j)$, these are not the positions of the three minima of the sum (1), because each minimum is slightly shifted by the tails of the other two Gaussians. Thus, to place the three minima at desired phase locations (q_j,p_j) in the q-p plane, one must choose the nominal positions $(\hat{q}_j,\hat{p}_j)$ so as to satisfy the six equations

$$\frac{\partial F}{\partial q}(q_j,p_j)=\frac{\partial F}{\partial p}(q_j,p_j)=0 . \tag{2}$$

We find the nominal positions by Newton iteration, starting from the desired phase positions.

Figure 1 illustrates the placement of the three phases in the q-p plane. We take well 0, which represents the liquid phase, to be at $(q_0,p_0)=(1,0)$. Well 2, which represents the stable solid phase is at $(q_2,p_2)=(-1,0)$. Well 1, which represents the metastable solid phase, is at a variable position (q_1,p_1). We shall focus much of our attention on the evolution of the nature of the splitting transition as the position of well 1 is varied.

The free energy (1) contains three control parameters h_j, which describe the depth of the well corresponding to each of the three phases. Since we want to describe the effect of temperature quenches, we parametrize variations

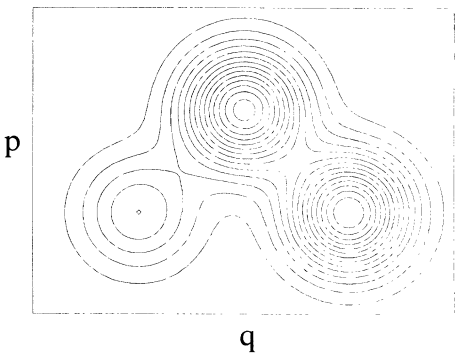

FIG. 1. Contour plot of the free energy $F(q,p)$ showing three wells and two saddle points. Here, the three wells are located at $(q_0,p_0)=(-1,0)$, $(q_1,p_1)=(0,1)$, and $(q_2,p_2)=(1,0)$ with heights $h_0=1.0$, $h_1=2.9$, and $h_2=3.0$.

of the potential (1) by a single control parameter h via

$$h_0=1, \quad h_1=h-0.1, \quad h_2=h \ . \tag{3}$$

Just as the minima of (1) are located near but not at the nominal positions $(\hat{q}_j,\hat{p}_j)$, so too the actual depths of the three wells are slightly different from h_j, the amplitudes of the individual Gaussians. Thus phases 0 and 2 (the liquid and stable solid) are in equilibrium at $h\approx 1$. For $h\gtrsim 1$, the stable solid phase grows into the liquid. The specific parametrization in Eq. (3), while arbitrary, takes into account that the free energy of the liquid phases normally varies with temperature more rapidly than does that of either of the two solid phases. (The existence of solid-solid phase transitions means that the difference between h_1 and h_2 must vary with temperature. Here, we neglect that variation with respect to that between h_0 and either h_1 or h_2). We then have that $h-1$ is roughly proportional to $(T_{20}-T)$ with T the growth temperature and T_{20} the 20 coexistence temperature. Thus $v_{20}=0$ at $h\approx 1$. (See Fig. 6.) Note that the depth of the well representing phase 1 is chosen so that it is always metastable with respect to phase 2.

In addition to three minima, the free energy defined by (1) has either one maximum and three saddle points, or, more usually, no maximum and two saddle points (see Fig. 1). When two minima are sufficiently close or of sufficiently different heights, one of them may merge with the saddle separating the two minima and disappear. According to our parametrization (3), the well at phase 2 is always lowest, so that only phases 0 or 1 may disappear. In phase-transition theory, such a point is known as a spinodal. At the spinodal point, the given phase is under- or supercooled so much that it becomes thermodynamically unstable. In our discussion below, we shall see that the range of the control parameter governing the relative depths of the three minima is often limited by spinodal points. For the real solid-liquid transition, no spinodal has ever been observed. Strongly undercooled liquids become glasses before the spinodal point, and surface melting implies that solids cannot be more than slightly superheated. So, in practice, temperature variations are bounded on the low end by the glass transition and on the high end by surface melting.

For small gradients in the order parameter, the full free energy may be written

$$\mathcal{F}[q(x,t),p(x,t)]=\int_{-\infty}^{\infty}dx\left\{F(z,p)+\frac{1}{2}\xi_q^2\left[\frac{\partial q(x,t)}{\partial x}\right]^2+\frac{1}{2}\xi_p^2\left[\frac{\partial p(x,t)}{\partial x}\right]^2\right\}, \tag{4}$$

where ξ_q and ξ_p are microscopic correlation lengths. The equations of motion for the two order parameters are then given by a set of coupled Landau-Ginzburg equations [25]

$$\begin{aligned}\tau_q\frac{\partial q(x,t)}{\partial t}&=-\frac{\delta\mathcal{F}[q,p]}{\delta q(x,t)}+\eta_q(x,t)\ ,\\ \tau_p\frac{\partial p(x,t)}{\partial t}&=-\frac{\delta\mathcal{F}[q,p]}{\delta p(x,t)}+\eta_p(x,t)\ ,\end{aligned} \tag{5}$$

where τ_q and τ_p set the time scales for the order parameters q and p to relax to equilibrium and the $\eta(x,t)$ are stochastic terms representing the effects of thermal fluctuations. We set $\eta_q=\eta_p=0$ because we are interested in the growth of fronts rather than their nucleation. In general, τ will depend on p, q, and the temperature, but here we shall assume $\tau_q=\tau_p=\tau$ to be constant. In addition, we set $\xi_q=\xi_p=\xi$. Scaling τ and ξ out of Eqs. (5), we have

$$\begin{aligned}\frac{\partial q}{\partial t}(x,t)&=\frac{\partial^2 q}{\partial x^2}-\frac{\partial F}{\partial q}\ ,\\ \frac{\partial p}{\partial t}(x,t)&=\frac{\partial^2 p}{\partial x^2}-\frac{\partial F}{\partial p}\ .\end{aligned} \tag{6}$$

We shall primarily look for constant-velocity solutions that are stationary in a moving frame defined by $x\to x-vt, t\to t$. (We shall sometimes refer to these as steady solutions.) Then $\partial q/\partial t\to -v\,dq/dx$, where v is the unknown front velocity. In this new frame, Eqs. (6) become

$$\begin{aligned}\frac{d^2q}{dx^2}+v\frac{dq}{dx}-\frac{\partial F}{\partial q}&=0\ ,\\ \frac{d^2p}{dx^2}+v\frac{dp}{dx}-\frac{\partial F}{\partial p}&=0\ .\end{aligned} \tag{7}$$

The boundary conditions to Eqs. (6) or (7) are that q and p adopt values corresponding to local equilibrium at $x=\pm\infty$. Specifically, a front propagating between phase i and phase j satisfies

$$\begin{aligned}q(-\infty,t)&=q_i, \quad p(-\infty,t)=p_i\ ,\\ q(+\infty,t)&=q_j, \quad p(+\infty,t)=p_j\ .\end{aligned} \tag{8}$$

By multiplying Eqs. (7) by dq/dx and dp/dx, respectively, adding the two equations, and integrating over x, one finds that the velocity v_{ij} of a front propagating between phase i and phase j is

$$v_{ij}=\frac{\Delta F_{ij}}{\sigma_{ij}}\ , \tag{9}$$

where

$$\Delta F_{ij}=F(q_j,p_j)-F(q_i,p_i) \tag{10}$$

and

$$\sigma_{ij}=\int_{-\infty}^{\infty}\left[\left(\frac{dq}{dx}\right)^2+\left(\frac{dp}{dx}\right)^2\right]dx\ . \tag{11}$$

F_{ij} is the free-energy difference between phases i and j, and σ_{ij} is proportional to the surface tension between phases i and j. Our convention is that phase i propagates from $x=-\infty$ to $+\infty$. Equation (10) implies that $v_{ji}=-v_{ij}$. Equation (9) does not give the velocity explicitly because the surface tension depends on the profiles $q(x)$ and $p(x)$, which in turn depend on v. However, near equilibrium, the order-parameter profiles do not vary much with velocity and may be well approximated by their $v=0$ solutions. [When $v=0$, Eqs. (7) have a first integral.]

We shall often use the "width" w to characterize the different steady-state 20 front solutions. The width is defined by exclusion and measures the portion of a trajectory that is near neither phase 0 nor phase 2. When phase 1 is placed at the origin, midway between phase 0 at $q_0=-1$ and phase 2 at $q_2=1$, we can define "near phase j" to be $|q-q_j|<\frac{1}{4}$ for $j=0$ or 2. We then define the width w by the difference $|x(q=\frac{3}{4})-x(q=-\frac{3}{4})|$, where $x(q)$ is the position at which the order parameter takes the value q. Generalizing this definition to an arbitrary placement of phase 1 on the q-p plane requires some care. Setting l_{ij} to be the Euclidean distance between phases i and j, we define "near phase j" to mean within a circle of radius $\frac{1}{4}l_{1j}$ centered on phase j. (See Fig. 2.) That is, we define the leading edge of the front to be the x value corresponding to the intersection of the solution with a circle of radius $\frac{1}{4}l_{10}$ centered on phase 0. The trailing edge is defined analogously using a circle of radius $\frac{1}{4}l_{21}$ centered on phase 2. The width is then the difference between these two x values.

As has been recognized many times before, the solutions to Eqs. (7) are most easily found by appealing to a mechanical analogy [26]: The order-parameter profiles $q(x)$ and $p(x)$ are interpreted as the x and y coordinates of a unit-mass particle moving in a potential $-F$ with a linear damping coefficient v. The wells (minima) of the free energy F become hills (maxima) of the potential $-F$; see Fig. 6. The front profile is the motion of a particle that starts on top of a potential hill representing one of the three stable phases. It slides down the hill starting at "time" $x=-\infty$ and just reaches the top of another hill (another phase) at "time" $x=+\infty$, as illustrated in the lower part of Fig. 6. Because the boundary conditions (8) imply that $dq/dx=dp/dx=0$ at $x=\pm\infty$, the "velocity" of the particle at the beginning and end of the trajectory must be zero. If the two hills have equal heights (i.e., if the two phases have the same free energy), then the only trajectory connecting the two phases will be one without friction, so that $v=0$. In other words, the front is stationary when the two phases are in equilibrium. If one of the phases has a lower free energy than the other, the two hills will have different heights, and a trajectory connecting the two hills will exist only if there is damping, i.e., only if the front moves, creating more of one phase at the expense of the other. Unlike in ordinary mechanics, negative damping permits a particle to move from a lower to a higher hill, increasing its potential energy; this corresponds merely to the front moving from right to left. Because we will use the mechanical analogy extensively in what follows, we will generally refer to phases 0, 1, and 2 as hills rather than as wells.

III. ONE ORDER PARAMETER

In this section, we set the position of hill 1, (q_1,p_1), to the origin. Hill 1 is then midway between hills 2 and 0, which are at $(-1,0)$ and $(1,0)$ respectively. Because the three hills and the two saddles lie on the q axis, there is effectively only one order parameter: all solutions have $p(x)=0$. Except for the choice of Gaussian hills rather than polynomial hills, this case is essentially that studied previously [9]. The equations we study in this simpler case of one order parameter are essentially those studied by Fife and McLeod in an earlier work on reaction-diffusion equations [17]. The values of h that we may consider are limited by two spinodal points: $h\equiv h_{\mathrm{sp}\,1}=0.382$, at which hill 1 is so low that it disappears and $h\equiv h_{\mathrm{sp}\,0}=3.535$, at which hill 0 disappears.

In Fig. 3, we plot profiles of $q(x)$ for two values of the control parameter h. Near $h=1$, q goes directly from phase 2 to phase 0 via an approximate tanh function. As h is increased, a shelf around $q=1$ forms. Figure 4(a) shows the width of this shelf w as a function of h. As $h\to h_{\mathrm{div}}=1.141$, w diverges logarithmically. [See the enlarged portion in Fig. 4(b).] For $h\lesssim h_{\mathrm{div}}$, the shelf around $q=0$ is large enough that we may consider it to be a macroscopic region of phase 1. Although we began with a single front separating phases 2 and 0, we now have two fronts, the first separating phases 2 and 1, and the second separating phases 1 and 0. Time-dependent simulations show all of these 20 solutions to be stable. At $h=h_{\mathrm{div}}$, the profile can be considered to be a concatena-

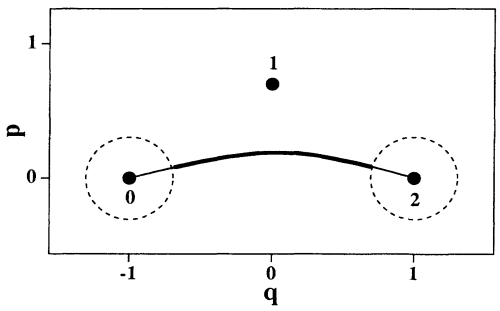

FIG. 2. Definition of the width of the 20 front. The radius of the dashed circles around phases 0 and 2 is $\frac{1}{4}$ the distance between phases 0 and 1 and between 2 and 1, respectively. The width is defined to be the extent (over x) of the 20 trajectory lying between the two circles. In the figure, that part is traced in a heavy line.

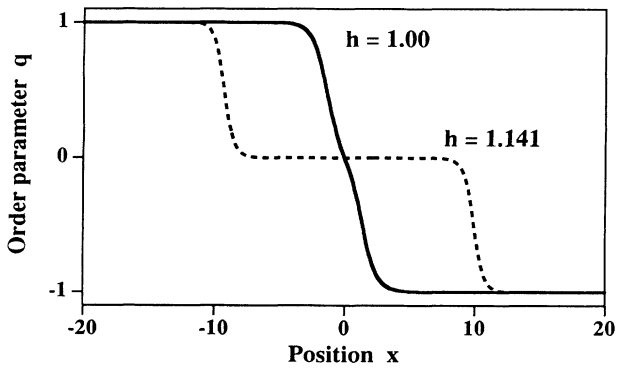

FIG. 3. Order-parameter profiles $q(x)$ for the one-order-parameter case $(q_1,p_1)=(0,0)$. The narrow profile is for $h=100$, where the 20 front is stationary. A shelf around $q=q_1=0$ develops as $h\to h_{\mathrm{div}}=1.142$.

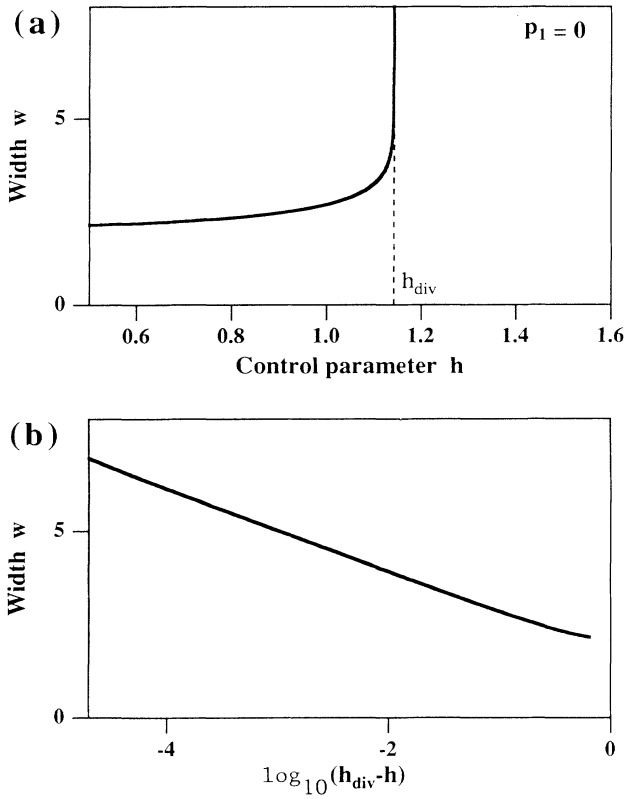

FIG. 4. (a) Width w of the 20 front vs h when $(q_1,p_1)=(0,0)$. (b) Semilog logarithmic plot of the same front widths, showing that the divergence is logarithmic.

tion of a 21 and a 10 front. For $h > h_{div}$, an initial 20 front widens steadily over time, as shown in Fig. 5(a). The time-dependent profile of Fig. 5(b) resembles the stationary profile of equal width shown in Fig. 3.

To understand this behavior, we obtain the velocities of the three possible front solutions (10, 21, and 20) by using the appropriate boundary conditions (8). We show these as a function of h in Fig. 6. The three velocities $v_{10}(h)$, $v_{21}(h)$, and $v_{20}(h)$ all intersect at h_{div}. The 10 and 21 fronts, unlike the 20 front, continue to exist for $h > h_{div}$. For $h > h_{div}$, the 10 front travels faster than the 21 front. Indeed, in time-dependent simulations dw/dt asymptotically approaches $v_{10}-v_{21}$, confirming the picture of the 20 front as separate 21 and 10 fronts. Roughly speaking, when $v_{21} > v_{10}$, the trailing edge of the front moves faster than the leading edge, and the 20 profile propagates as a bound state with a velocity intermediate between v_{21} and v_{10}. When $v_{10} > v_{21}$, the 20 front splits into two pieces, each of which moves with its own velocity. (See also [17].)

To understand why there is no 20 steady-state front when $h > h_{div}$, we use the mechanical analogy of particles moving in a potential (as illustrated in the lower part of Fig. 6) to demonstrate the inequality

$$v_{10} < v_{20} < v_{21} \ . \tag{12}$$

Compare two different particle trajectories each beginning at the rightmost hill 2, one of which stops at hill 1, the other continuing on to the leftmost hill 0. (Both trajectories begin and end with the zero velocity $q_x = 0$ required by the mechanical analogy.) In order for the particle to continue on to hill 0, it must cross over hill 1 with a nonzero velocity. Hence it has been subjected to less friction than the particle that stopped at hill 1. Recalling that friction corresponds to front velocity, we have $v_{20} < v_{21}$. Now compare two trajectories terminating on hill 0, beginning at hills 1 and 2. The trajectory that begins at hill 2 crosses over hill 1 with a nonzero velocity. The friction necessary to stop its motion at hill 0 is therefore greater than if it had begun on hill 1 with zero velocity, implying that $v_{20} > v_{10}$. When v_{10} becomes greater than v_{21} at h_{div}, the 20 front ceases to exist.

Three potentials $-F(q,0)$, for $h < h_{div}$, $h = h_{div}$, and $h > h_{div}$, are shown in the lower part of Fig. 6. The first potential is at the coexistence value $h = 1$, and we have $v_{20} = 0$ and $v_{10} = -v_{21}$. That is, hills 0 and 2 have equal heights, so no friction is required to travel between them. Traveling from the shorter hill 1 to either of the other

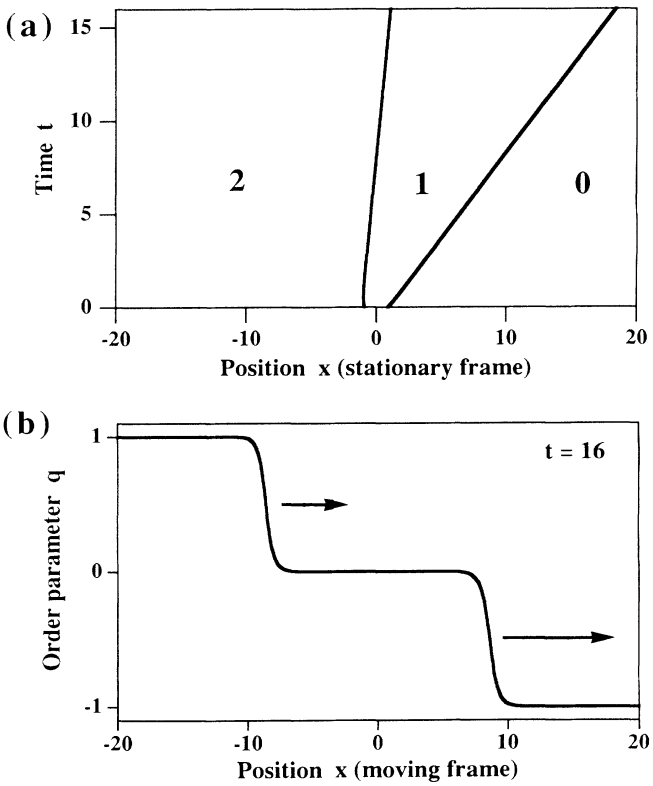

FIG. 5. (a) Space-time diagram of the motion of the 10 and 21 fronts for $h = 1.6 > h_{div}$. Initial condition is the stationary 20 solution at $h = 1.00$. Note the ever-widening region of phase 1. (b) Time-dependent 20 profile at $t = 16$, same conditions as in (a). Profile is shown in a moving frame, space-time diagram in the stationary frame. The velocities of the leading edge (10 front) and trailing edge (21 front) are shown schematically by arrows.

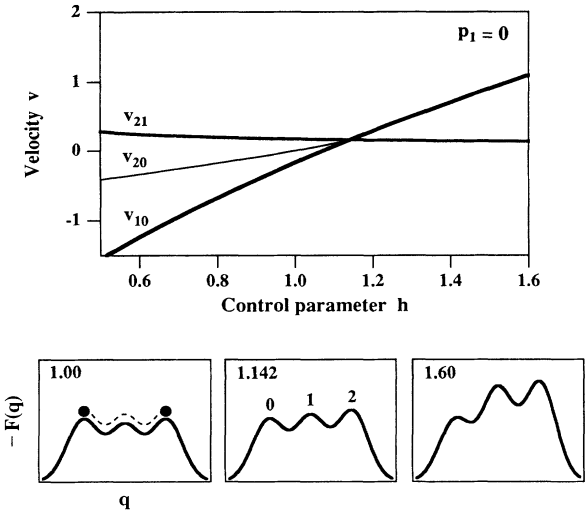

FIG. 6. Velocities of the 20, 21, and 10 fronts as a function of the control parameter h, satisfying $v_{10} < v_{20} < v_{21}$. Velocities v_{21} and v_{10} cross at h_{div}, above which the 20 solution ceases to exist. Below are three curves showing the negative of the free energy $-F(q)$ as a function of the order parameter q. For $h = 1.00$, hills 2 and 0 are of equal heights: the 20 front is stationary and $v_{10} = -v_{21}$. For $h = 1.142 = h_{div}$, we have $v_{10} = v_{20} = v_{21}$. For $h = 1.60 > h_{div}$, $v_{10} > v21$ and no 20 solution is possible. The motion of a particle in the mechanical analogy is illustrated schematically on the $h = 1.00$ potential.

two hills requires friction, whose value is the negative of that of the time-reversed trajectory. The second potential is at $h = h_{div}$, where $v_{21} = v_{10}$ so that the two trajectories may be concatenated to form a single 20 trajectory. The third potential is at $h > h_{div.}$. In that case, any friction that allows the particle to pass from hill 2, passing over hill 1, will be too small to stop the particle by hill 0.

The mechanical analogy can also by used to show that the 20 trajectory, if it exists, is unique. Let v^* be the friction corresponding to a 20 trajectory. Then, if we increase the friction, the trajectory will oscillate back and forth before settling in the minimum between hills 1 and 0, or that between hills 2 and 1. If, on the other hand, we decrease the friction, the trajectory will have a finite velocity at the top of hill 0 and will continue down the other side and go off to $-\infty$. Thus v^* is the only possible value of the friction, and the solution is unique.

Both of these arguments assume that the trajectory connecting hills 2 and 0 passes over hill 1, and are therefore particular to one order parameter. We will see that in the two-order-parameter case, the trajectories are not unique, and the inequality $v_{10} < v_{20} < v_{21}$ is not always obeyed.

IV. TWO ORDER PARAMETERS

In this section, we look at front motion for the case where the metastable phase 1 is located at a position $p_1 > 0$ with $q_1 = 0$. The three phases now form a symmetric triangle, as illustrated in Fig. 1. Because of the way in which we parametrize variations in the free energies of the three phases via (3) (the height of hill 2 is varied, but that of hill 0 is fixed), this does not imply any special symmetry for the potential $F(q,p)$. (See Fig. 1.) We thus expect the phenomena observed with $q_1 = 0$ to persist at other values of q_1. As p_1 is increased, we encounter four qualitatively different regimes, which will be illustrated by the graphs of 20 front widths versus h.

A. Region I

In region I, which extends over $0 \leq p_1 < 0.819$, the behavior of the splitting transition is similar to that observed for one order parameter. A front corresponds to a rapid variation in both $q(x)$ and $p(x)$. Narrow and wide fronts are illustrated in Fig. 7, where $p_1 = 0.70$. The wide profile has not only a shelf in q around $q = q_1 = 0$, but also a shelf in p around $p = p_1 = 0.70$. A graph of width w as a function of h is shown as the upper part of Fig. 8 for the same value of p_1. As in the one-parameter case, which, indeed, is a special case of region I, all solutions along this branch are stable. The width of the front diverges logarithmically as $h \to h_{div} = 1.182$. For $h > h_{div}$, the 20 front splits into separating 21 and 10 fronts.

The divergence h_{div} again coincides with the triple intersection of the velocities of 10, 21, and 20 fronts. The lower portion of Fig. 8 shows the evolution of the 20 front as h approaches h_{div}. Here, solutions are represented in the q-p plane, the curves being parametrized by the

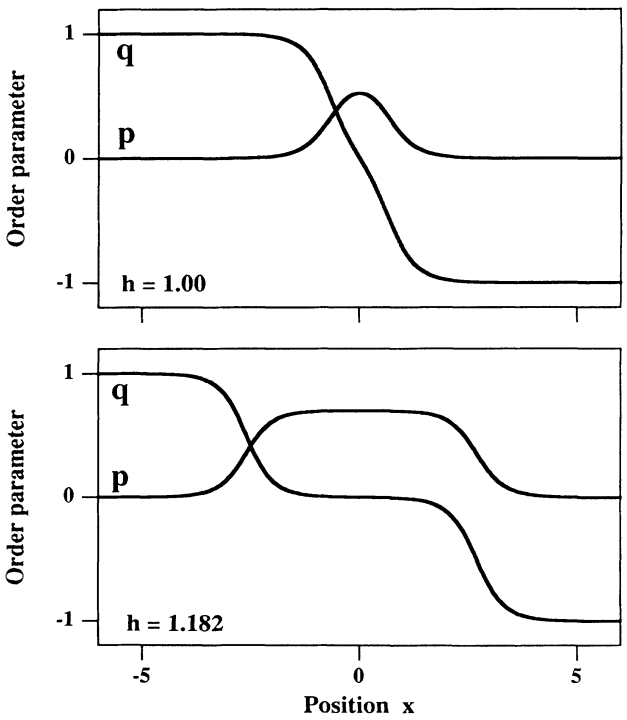

FIG. 7. Order parameter profiles in region I for $p_1 = 0.70$. The profile at $h = 1.00$ ($v_{20} = 0$), shows a narrow 20 front with little trace of phase 1, while that at $h = 1.182 = h_{div}$ shows a wide 20 front with a substantial region of phase 1.

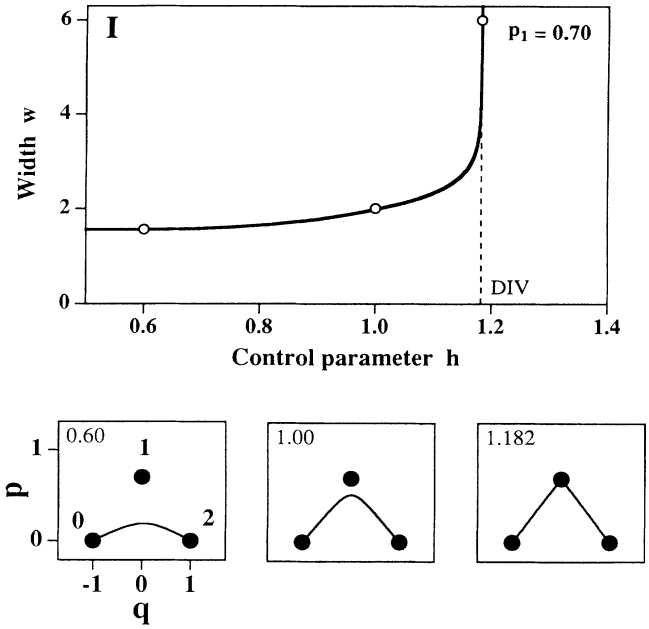

FIG. 8. Front behavior in region I for $p_1=0.70$. The width of the front diverges logarithmically as $h\to h_{\rm div}$. Parametric plots of the front in the q-p plane are shown for different values of the control parameter h corresponding to the hollow circles in the w vs h plot. As $h\to h_{\rm div}=1.182$, the front converges towards a concatenation of 21 and 10 trajectories with a sharp angle at phase 1.

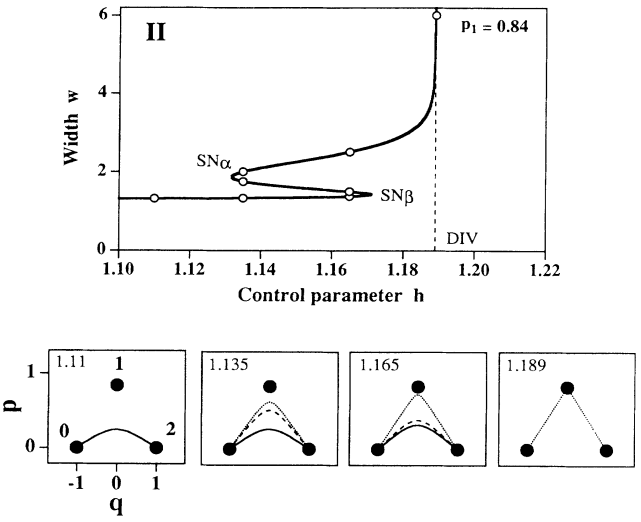

FIG. 9. Front behavior in region II for $p_1=0.84$. Two saddle-node bifurcations SN_α and SN_β cause a region of hysteresis in the front width to develop. Corresponding to the hollow circles are parametric plots, illustrating the evolution of front solutions. At $h=1.11$, the solid curve is the unique and stable 20 solution. By $h=1.135$, an additional pair of solutions, one stable (dotted) and one unstable (dashed) has been created via SN_α. The plot at $h=1.165$ immediately precedes the destruction of a pair of solutions (solid and dashed curves) via SN_β. The single remaining dotted solution at $h=1.189$ disappears by diverging at DIV.

spatial variable x. In the language of the mechanical analogy, the 20 trajectory at $h_{\rm div}$ is again a concatenation of the 21 and 10 trajectories, since the friction of all three is the same. The concatenated trajectory is the limiting case of a 20 trajectory where the particle spends an ever-longer time and makes an ever-sharper turn near phase 1.

B. Region II

At $p_1\gtrsim 0.819$ the w-h curve develops two saddle-node bifurcations near $h=1.10$, which we denote by SN_α and SN_β. For region II, i.e., $0.819<p_1<0.845$, we have $h_{SN\alpha}<h_{SN\beta}<h_{\rm div}$. Figure 9 shows a plot of w as a function of h for $p_1=0.84$, accompanied by parametrized q-p representations of the profiles. We see that three solutions exist over the range $h_{SN\alpha}<h<h_{SN\beta}$. To understand how multiple solutions can arise, consider the extreme case of thin but widely separated hills. In this case, one expects two solutions, one directly connecting hills 0 and 2, the other bouncing off hill 1. They will exist whenever the three hills are well-enough separated, i.e., whenever the hill widths are much smaller than the distances between them.

Since all of the steady 20 solutions are stable for p_1 belonging to region I, we may argue by continuity in p_1 that solutions far from the new saddle-node bifurcations continue to be stable in region II. Specifically, the low-width solution that exists for $h<h_{SN\beta}$ and the high-width solution that exists for $h_{SN\alpha}<h<h_{\rm div}$ are both stable. Because the stability of the solution branch changes if and only if a saddle-node bifurcation is encountered, the intermediate-width solution that exists for $h_{SN\alpha}<h<h_{SN\beta}$ is unstable. In this range of h, there are two stable solutions, and one could in principle observe hysteretic transitions between them. But since the upper and lower branches are both finite-width solutions, it would be difficult in practice to detect such transitions. For this reason, we shall continue to focus on the splitting transition from a steady, finite front to an unsteady, ever-widening front. In region II, this transition occurs at $h=h_{\rm div}$, with the same qualitative behavior as in region I.

C. Region III

The location of the second saddle-node bifurcation $h_{SN\beta}$ increases rapidly with p_1. At $p_1=0.845$, the saddle node crosses the divergence: $h_{SN\beta}=h_{\rm div}=1.189$. This marks the beginning of region III, which extends over $0.845<p_1<1.146$. For each p_1 in region III, the inequality $h_{SN\alpha}<h_{\rm div}<h_{SN\beta}<h_{sp0}$ is satisfied. A typical case, $p_1=0.88$, is shown in Fig. 10. As before, continuity in p_1 dictates the stability of the solutions.

In region III, the multiple solutions imply that the splitting transition is hysteretic. For $h<h_{\rm div}$, finite-width 20 solutions will not split. For $h_{\rm div}<h<h_{SN\beta}$, a large

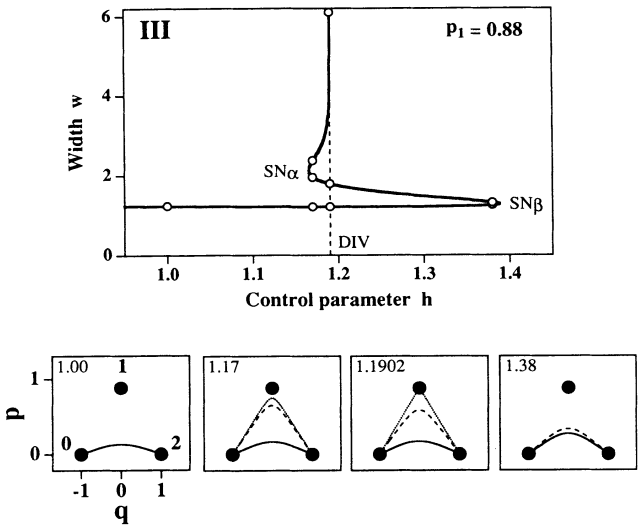

FIG. 10. Front behavior in region III for $p_1 = 0.88$. This region differs from region II in that the second saddle-node bifurcation SN_β now occurs after DIV, making the splitting transition hysteretic. Parametric curves correspond to the open circles, with solid and dotted curves representing stable solutions and the dashed curve an unstable one.

enough perturbation will split the stable 20 solution. The resulting 21 and 10 fronts then separate with a finite asymptotic velocity, roughly proportional to $(h - h_{\rm div})$. As $h \to h_{{\rm SN}\beta}$, the perturbation required to split the front decreases, until it vanishes at $h_{{\rm SN}\beta}$. For $h > h_{{\rm SN}\beta}$, any front will split. If the control parameter is subsequently reduced, the 20 front will not reappear until $h < h_{\rm div}$, meaning that the range of observable hysteresis is $h_{{\rm SN}\beta} - h_{\rm div}$. Thermal fluctuations, which we have been neglecting, will reduce the range of hysteresis actually observed.

Figure 11 shows the velocity of the 10, 21, and 20 solutions as functions of h. The divergent trajectory of infinite width at $h_{\rm div}$ is always the concatenation of 21 and 10 solutions with equal velocities $v_{21} = v_{10}$. (See the parametrized trajectories of Figs. 8–10.) In region III, 20 solutions exist for $h > h_{\rm div}$ where $v_{10} > v_{21}$; hence it is clear that inequality $v_{10} < v_{20} < v_{21}$ is violated. However, the inequality does continue to hold *for 20 trajectories that pass sufficiently close to hill 1.* The saddle-node bifurcation always occurs at $h_{{\rm SN}\alpha} < h_{\rm div}$ and so $w(h)$ approaches the divergence line from the left. [Were $h_{{\rm SN}\alpha}$ to cross $h_{\rm div}$, it would disappear and an infinite portion of the $w(h)$ curve would change its character and stability.] Solutions of sufficiently high width always satisfy $h \lesssim h_{\rm div}$ and $v_{10} < v_{20} < v_{21}$.

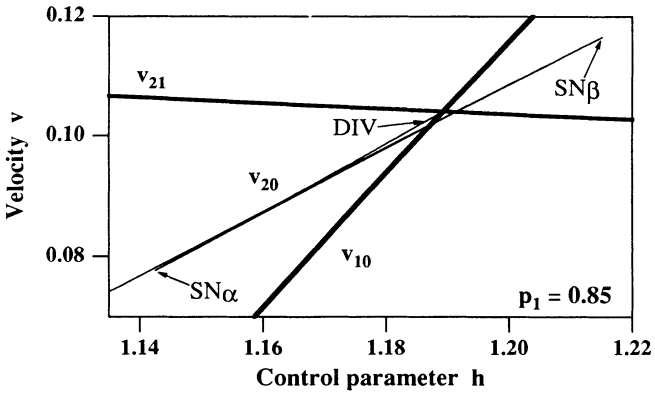

FIG. 11. Velocity curves vs h for region III for $p_1 = 0.85$. In contrast to Fig. 6, the v_{20} curve is not sandwiched between v_{10} and v_{21}. After turning sharply at the saddle-nodes SN_β and SN_α, v_{20} does eventually approach asymptotically the intersection between the v_{10} and v_{21} curves as in the one-order-parameter case.

D. Region IV

At $p_1 = 1.146$, the second saddle-node bifurcation meets the hill 0 spinodal: $h_{{\rm SN}\beta} = h_{{\rm sp}\,0} \approx 140$. This marks the beginning of region IV. For $h > h_{{\rm sp}0}$, phase 0 is unstable and spontaneously decays to phases 1 or 2. At that point, it is no longer meaningful to describe fronts involving phase 0. (In fact, thermal fluctuations make this true at values of h slightly less than $h_{{\rm sp}0}$.) This case is illustrated in Fig. 12, for $p_1 = 1.20$. What distinguishes the splitting transition in region IV is that a finite perturbation is needed to split a 20 front for any permissible value of h. The size of the required perturbation grows as we go further out into region IV, i.e., with increasing p_1. At some point, it will be so large as to make the splitting transition impossible in practice. Region IV extends over $p_1 > 1.146$.

E. Summary of regions I–IV

We have seen that, for increasing p_1, the splitting transition is continuous (regions I and II), then hysteretic (region III), then finite amplitude (region IV). This evolution is summarized in Fig. 13, which traces as a function of p_1 the critical values of h: the spinodals at $h_{{\rm sp}\,1}$ and

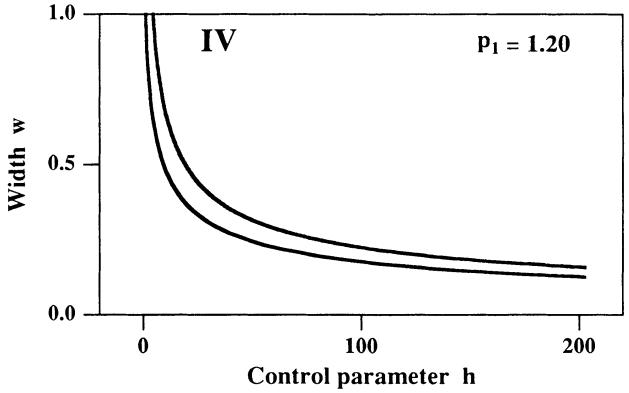

FIG. 12. Front behavior in region IV for $p_1 = 1.20$. Here, the w-h curves intersect the spinodal line $h_{{\rm sp}0}$. Thus the two separate branches of the w-h curve never meet.

h_{sp0}, the saddle-nodes at $h_{SN\alpha}$ and $h_{SN\beta}$, and the divergence h_{div}. The successive intersections of $h_{SN\beta}$ with the other critical curves delimit the four regions. As previously stated, the intersection of $h_{SN\beta}$ with $h_{SN\alpha}$ separates regions I and II and takes place at $p_1=0.819$. Its intersection with h_{div} at $p_1=0.845$ separates regions II and III, and its intersection with h_{sp0} at $p_1=1.146$ separates regions III and IV. Each of these p_1 values is thus a point of codimension two, where two critical h curves intersect.

Generically, two saddle-node bifurcations meet in a cusp [27], which can be seen in the expanded graph in the lower part of Fig. 13. Another feature visible in Fig. 13 is that $h_{SN\beta}$ intersects the spinodal line h_{sp0} transversely. We see that $h_{SN\alpha}$ approaches h_{div} asymptotically from below as $p_1\to\infty$. Recall that this implies that the divergence is always approached from below, which in turn implies that inequality (12) is satisfied for sufficiently wide 20 trajectories.

F. Other angles

We now allow the position of hill 1 to vary over the entire q-p plane, extending our results to $q_1\neq 0$. It is convenient to describe the position of hill 1 by polar coordinates $r=\sqrt{q_1^2+p_1^2}$ and $\tan\theta=p_1/q_1$. Thus the cases described above all had angle $\theta=\pi/2$, with p_1 playing the role of the radius r. Figure 14 shows a collage of graphs similar to Fig. 13. Critical h values are plotted as a function of r, but now for a variety of angles θ. Placing hill 1 at $+p_1$ or at $-p_1$ should lead to the same scenario (interchanging $p\to -p$), which implies a symmetry between $(\pi+\theta)$ and $(\pi-\theta)$. We use this to show θ and $(\pi-\theta)$ on one graph, with the understanding that these two angles actually comprise a single diameter.

Away from $\theta=0$ and π, the qualitative features of the $\pi/2$ scenario persist in Fig. 14. The width of the 20 solution continues to diverge at the intersection of $v_{10}(h)$ and

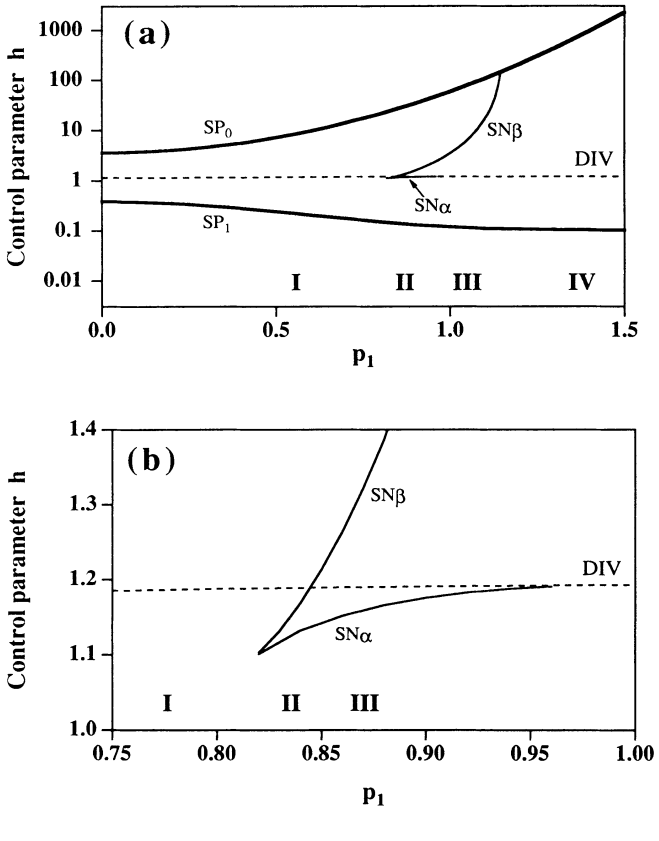

FIG. 13. Critical curves as a function of p_1 for hill 1 located at $q_1=0$. Shown are the spinodals SP_1 and SP_0 (heavy solid curves), the saddle-nodes SN_α and SN_β (light solid curves), and the divergence DIV (dashed curve). Intersections of SN_β with other critical curves divide the p_1 axis into regions I–IV. (b) Inset showing the intersection of the two saddle-node bifurcation curves in a cusp, as expected generically. The SN_α curve approaches DIV asymptotically, while the SN_β curve intersects DIV transversely.

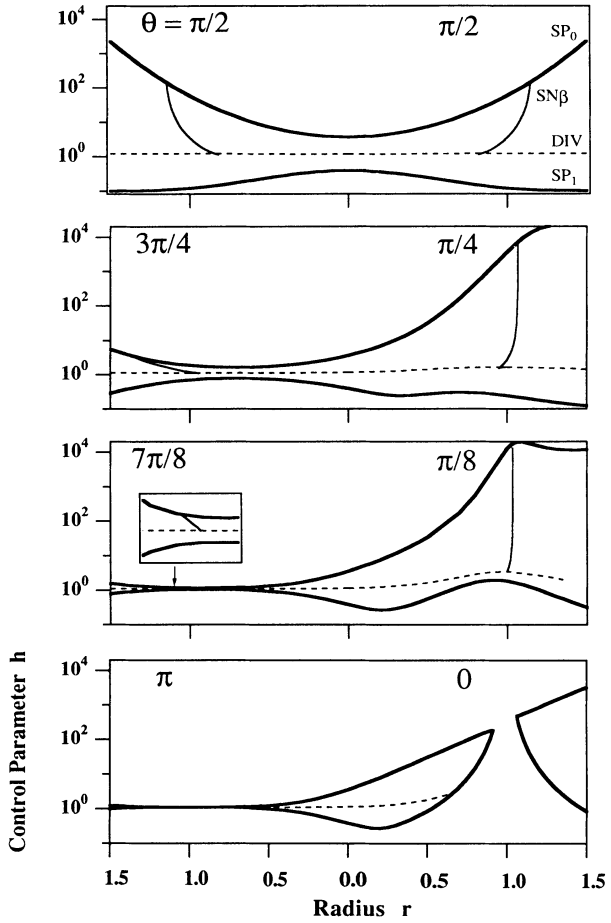

FIG. 14. Critical curves as a function of r for representative values of θ. Symmetry allows angles θ and $\pi-\theta$ to be plotted along their common diameter. Spinodals are heavy solid curves, DIV the dashed curves, SN_β the light solid curve (SN_α is too close to DIV to be shown). For each angle, intersections of SN_β with other critical curves divide the r axis into regions I–IV. The $\pi/2$ scenario remains qualitatively unchanged except near $\theta=0$, where SP_1 cuts off DIV.

$v_{21}(h)$ which remains at $h_{\rm div}\approx 1.1$. The saddle-node bifurcation curve $h_{{\rm SN}\alpha}(r)$ cannot be seen on the figure, but it continues to join $h_{{\rm SN}\beta}(r)$ at a cusp and to approach $h_{\rm div}(r)$ asymptotically from below. For each angle θ away from 0 or π, regions I–IV are separated by codimension-two points, which we denote by $r_{\rm I,II}(\theta)$, $r_{\rm II,III}(\theta)$, and $r_{\rm III,IV}(\theta)$. As in the $\pi/2$ case, these critical radii are defined by the successive intersections of $h_{{\rm SN}\beta}(r)$ with the other critical curves $h_{{\rm SN}\alpha}(r)$, $h_{\rm div}(r)$, and $h_{\rm sp0}(r)$.

As we increase θ from $\theta=\pi/2$, the saddle-node curve $h_{{\rm SN}\beta}$ becomes flatter, initially enlarging the radial extent of regions II and III. As $\theta\to\pi$, however, the effect of flattening is soon counterbalanced by the drastic fall in spinodal $h_{\rm sp0}$, which precipitates the beginning of region IV. As $h_{\rm sp0}$ falls, $h_{\rm sp1}$ rises. For $\theta\approx\pi$, hills 0 and 1 are very close together and separated by a shallow saddle: only small h variations are necessary for one of the hills to overwhelm the other. Near $\theta=\pi$, $h_{\rm div}$ passes through the narrow channel between the two spinodals. The saddle-node curves are also thus confined, and their extent in h and in r becomes infinitesimal. When $\theta=\pi$, the two spinodals meet at $r=1$, where the positions of hills 1 and 0 coincide and no height difference can preserve both hills. The reappearance of $h_{\rm div}$ for $r>1$ and $\theta=\pi$ can be understood via pictures similar to those in the lower part of Fig. 6, but with hill 1 to the left of hills 0 and 2. With this arrangement, it is solution 21 which is threatened by changes in h and which must obey a sandwiching inequality. The parametrization (3) implies that for $h\gtrsim h_{\rm div}$, there exists a trajectory which begins at 2, crosses 0, and continues leftwards almost to 1 before reversing direction and coming to rest again at 0. At $h=h_{\rm div}$ this trajectory is the concatenation of 21 and 10 trajectories with $v_{21}=v_{10}$.

The situation is quite different for small θ. We see from Fig. 14 that curve $h_{{\rm SN}\beta}$ becomes more vertical, intersecting the rising spinodal $h_{\rm sp0}$ at a steeper angle. The curve $h_{{\rm SN}\beta}$ extends over a small range of r and a large range of h; the transition between regions I and IV occurs over a small radius. For $\theta\to 0$ and $r\to 1$, the spinodal $h_{\rm sp1}$ rises to intersect and annihilate $h_{\rm div}$ and its accompanying saddle-node curves. We denote the region for which $h_{\rm div}$ no longer exists as region A and the critical radius separating regions I and A as $r_{\rm I,A}$. In region A, there are no steady 20 front solutions for h between the spinodals $h_{\rm sp1}$ and $h_{\rm sp0}$: any initial condition will split.

We can again use the mechanical analogy to gain insight into this behavior. For $\theta=0$ and $r>1$, the hills are ordered as 0,2,1. Because hill 2 is higher than hill 1, v_{21} must be positive. Because a 10 trajectory must pass over the higher hill 2, v_{10} must be negative. Hence the v_{21} and v_{10} can never cross and a divergent 20 trajectory which is the concatenation of 21 and 10 trajectories can never exist. Since our parametrization, Eq. (3), calls for the height difference between hills 2 and 1 to remain (approximately) 0.1, the difference between v_{21} and v_{10} also remains finite for $\theta=0$. We can therefore extend the region in which $v_{21}=v_{10}$ is forbidden to finite values of θ. This provides a heuristic explanation for the disappearance of $h_{\rm div}$ and the resulting breakdown in the splitting scenario at small values of θ. Many features of the evolution as $\theta\to\pi$ or 0 and $r\to 1$, i.e., as phase 1 approaches phase 0 or 2, are consequences of our particular parametrization and we shall not emphasize them further.

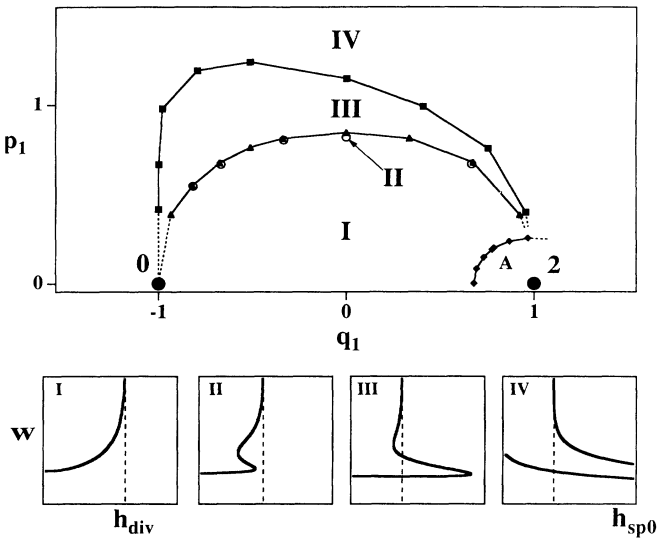

FIG. 15. Plot of regions I–IV and A in the q_1-p_1 plane. Boundaries are shown as lines joining the codimension-two points $r_{\rm I,II}(\theta)$ (circles), $r_{\rm II,III}(\theta)$ (triangles), $r_{\rm III,IV}(\theta)$ (squares), and $r_{\rm I,A}(\theta)$ (diamonds). Region II consists of a thin sliver, not visible on this scale. In region A there are no steady 20 fronts for the allowed h values. Dashed lines are hypothesized continuations of existing boundaries into the atypical regions where the two spinodals come together. Below are typical w vs h plots for the four regions.

In Fig. 15, we plot the codimension-two points collected from Fig. 14 as well as other intermediate angles. These partition the (q_1,p_1) plane into regions I–IV and A. Figure 15 summarizes all of our results, showing the phase-1 positions where the splitting transition is continuous, hysteretic, and finite amplitude.

V. DISCUSSION

A. Additional order parameters

We have seen in Sec. IV that for one order parameter, 20 trajectories must pass over hill 1 and, hence, that they are unique and obey the inequality $v_{10}<v_{20}<v_{21}$. For two order parameters, this is no longer true, and the splitting transition is qualitatively different as a result. Will additional order parameters change the two-order-parameter scenario? At first glance, the answer is no: for three phases, we can always define two order parameters whose coordinates span the plane defined by the three hill maxima. An analogy can be made to motion in the presence of three repelling bodies. A particle traveling from one repellor to another moves in the plane defined by the three repellors. Were it to escape from the plane, there would be no force to send it back.

However, the situation is subtler: if the free energy has saddle points that lie outside of the plane defined by the three maxima, then front trajectories can in fact deviate from the plane. To understand this, let us consider again the two-order-parameter case, where, by construction, motion is confined to the plane. Although one expects trajectories between two hills to lie within the triangle defined by the straight lines connecting the three hills, in fact, saddles outside the triangle can deflect the trajectories back in. We commonly observe this in our simulations. Similarly, saddles lying outside the order-parameter plane can deflect trajectories back into the plane. (See [13], pp. 57–64, 219–220, for a discussion.) In this case, we could replace our plane with a two-dimensional curved surface generated by the ensemble of front trajectories. In practice, of course, this surface would be hard to compute, and the more relevant question is whether projecting the motion onto the plane defined by the three maxima constitutes a good approximation. The saddles will be in the same plane as the maxima if the free energy is symmetric under reflection about that plane, a condition satisfied by a free-energy function that is the sum of spherically symmetric potentials. Therefore free-energy functions of the form (1) with many order parameters would still have trajectories confined to a plane. The only way for a saddle to be located off the plane defined by the three maxima is if the shape of each hill about its maximum is locally not a circular paraboloid. If, as seems reasonable, their anisotropy is small, then saddles will not lie far outside the plane. Front trajectories will then travel close to the plane and we expect that the splitting-transition scenario will not be strongly affected.

B. Parametrization of the free energy

In our discussion so far, we have adopted an apparently arbitrary parametrization of the free energy (potential), in which hill 0 had a fixed height of 1, hill 2 had an adjustable height h, and hill 1 was always $h-0.1$. In this section, we argue that such a parametrization is a reasonable description of the effects of varying temperature, provided that we set $(h-1)\propto(T_{20}-T)$. At the 20 coexistence temperature, phase 1 is by definition metastable. Since hills 0 and 2 are of equal height, we must have $v_{10}<0$ and $v_{21}>0$. Because the free energies of the two solid phases 1 and 2 descend in lock step with respect to that of the liquid phase 0, v_{10} will increase, while v_{21} will remain approximately constant. [Recall from Eqs. (9) and (10) that for small deviations from equilibrium, phase i propagates into phase j with $v_{ij}\propto\Delta F_{ij}$.] Eventually, we expect v_{10} to become larger than v_{21}, which is the necessary condition for front splitting.

This argument confirms the intuition that metastable phase are formed most easily when the metastable phase closely resembles the stable phase. Here, we see that "resembles" must be interpreted as having similar values of order parameters and having nearly equal free energies. If the metastable phase is too far away in free-energy space—if the distance between maxima greatly exceeds the hill widths—the phases will not "interact" and there will be no splitting transition. If the free energy of the metastable phase is much higher than that of the stable phase, the rule for splitting to occur, $v_{10}>v_{21}$, will not be satisfied.

C. Relation to surface melting and wetting transitions

The splitting transition is closely related to van der Waals models of surface melting. Near the triple point of a pure material, the solid-vapor interface can develop a thin liquid layer whose width diverges logarithmically as the triple point is approached [28]. Our equations are the same as those used in such models of surface melting, provided one changes the parametrization of hill heights so that $h_0=h_2=1$, $h_1=h$. In that case, $h=1$ would represent the triple point where phases 0, 1, and 2 coexist [29,30]. Our front splitting transition is thus the nonequilibrium generalization of surface melting. Note that nonequilibrium effects on surface melting have been previously considered [31]; however, since such effects are negligible in experiments on surface melting, their full implications were not pursued.

It is interesting to compare the criterion for surface melting with that for the splitting transition we have been discussing. For surface melting to occur, the necessary condition is that the solid-vapor surface tension σ_{20} equals the sum of solid-liquid σ_{21} and liquid-vapor σ_{10} surface tensions. For the splitting transition, the condition is that the liquid-stable front velocity v_{20} equal the stable-metastable v_{21} and the metastable-liquid v_{10} front velocities. The condition on interfacial tensions in surface melting may be traced to the requirement that the free energy be minimized. The condition on front velocities is one on the response functions. [The velocity is a response function since $v(h)$ gives the front velocity in response to the nonequilibrium stress represented by h.] In this case, we do not know of any function that is being minimized when the 20 front splits.

D. Applications to experiment

Splitting transitions ought to be present in both pattern-formation experiments and during phase transitions. In both cases, complications may occur.

For pattern-forming systems, several patterns may coexist over a small range of parameter space. For example, spatially uniform two-dimensional systems generically exhibit hexagon, line, and square patterns over small ranges of parameters. Experimental realizations include non-Boussinesq Bénard convection [32] and the Faraday instability of a vibrating liquid layer [33]. For such experiments, the splitting transition would correspond to the breakup of a moving domain wall separating two patterns. One complication is that the instabilities responsible for pattern formation are often supercritical bifurcations, which are analogous to mean-field second-order phase transitions. Because we have been discussing first-order phase transitions, the corresponding instabilities ought to be subcritical. The fronts between stable and unstable states created by a sudden control-parameter variation in the presence of a supercritical bifurcation

can still propagate but calculating their velocity is a subtle problem [19]. A second complication is that the amplitude equations describing instabilities are not always derivable from a potential. The equations may still be written in a form similar to the one we have studied here, but the coefficients will be complex. We have yet to study this case. A third, more obvious complication is that these patterns exist in two spatial dimensions, whereas our calculations are for one spatial dimension.

Although the splitting transition has not, to our knowledge, been observed in convection or the Faraday experiment, one of us has observed similar phenomena in a moving front separating twisted from nontwisted regions of a chiral nematic liquid crystal [34,35]. As the front velocity is increased, different patterns of twisted nematic are indeed left behind the front. Although systematic observations were not made at the time, the splitting transition is either second order or very nearly so in that case. One difficulty in analyzing this case is that, although the free energy may be expressed in terms of two nonconserved order parameters, the function itself is very complicated.

Another pattern-formation system where the splitting transition may have been observed is in moving nematic-isotropic interfaces of liquid crystals. Above a critical velocity, a region of twisted nematic detaches from the interface and leaves a triangular patch behind the interface [36–38]. Here, the detachment of the twisted-nematic region is strongly hysteretic as the nematic-isotropic front velocity is varied [39], so that this would be an example of a first-order splitting transition. We emphasize that although both of these experiments display behavior suggestive of splitting transitions, no quantitative analysis has yet been done.

For thermodynamic situations, there are two points to consider. The first is that most phase transitions involve conserved order parameters. Even the prototypical situation we referred to in the Introduction, the formation of graphite or diamond, requires a conserved order parameter to model the density difference between the two phases. Introducing conserved order parameters does not change the general form of free energy one considers but does change the equations of motion somewhat. Oxtoby and Harrowell, however, have recently considered the effects of density differences on the kinetics of solid-liquid interfaces and found them usually to be small [40]. A potentially more interesting situation is that of a binary mixture or alloy, where concentration is a conserved order parameter. In an alloy, Cahn has shown that there may be no unique ordering of the stability of different phases. For example, one may find circumstances where a given phase 2 cannot nucleate in the presence of metastable phase 0 but can in the presence of a different metastable phase 1, [41]. Thus, whether a front will split may depend on the detailed history and preparation of the sample.

The second point concerns practical experiments. One might wonder how fast, in real units, fronts must travel before they split. A rough answer is that in Eqs. (4) and (5), the only length scale is the bare correlation length ξ, and the only time scale is the microscopic relaxation time τ. For ordinary solids (e.g., metals), $\xi \approx 10^{-8}$ cm and $\tau \approx 10^{-12}$ sec. The length scale is characteristic of the thickness of the solid-liquid interface and is set by the lattice constant of the solid. The time scale can be thought of as roughly the mean time between collisions in the liquid, or, more to the point, the time it takes an atom on the liquid side of an advancing solid-liquid front to find its place in the solid phase. The characteristic front velocity is then about 10^4 cm/sec, which is indeed comparable to the solidification velocities achieved by techniques such as splat cooling.

Such rapid cooling rates make experiments difficult to control and interpret. Thus it is problematic to know whether some of the metastable phases created by splat cooling are in fact due to the splitting transition. Another approach is to search for systems where the scale velocity is smaller. The key observation is that materials made of larger molecules or having structures with larger repeat distances will have much slower relaxation times. Thus we anticipate that systems such as liquid crystals or copolymers, with their large molecules and high viscosities, may be good candidates to search for splitting instabilities.

VI. CONCLUSIONS

In summary, we have introduced a dynamical mechanism to explain the formation of metastable states. As stated in the Introduction, the splitting transition depends on two conditions. First, the velocity of the metastable-liquid front (v_{10}) must exceed that of the solid-metastable front (v_{21}). Second, given the condition on velocities, realistic initial conditions must lead to splitting. We have seen that the first condition should be satisfied for sufficiently large undercooling, while the second can be expected to hold if the metastable phase is close enough to the other two phases in order-parameter space.

Although the model of the splitting transition we have studied in this paper is still too simple to be compared directly to experiment, it does suggest a number of theoretical extensions and experimental projects that, together, will lead to stringent tests of the relevance of the kind of transition we have considered in this paper.

ACKNOWLEDGMENTS

We are grateful to Hartmut Löwen for his many contributions to the in-line case. We thank John W. Cahn, Tony Arrott, and Udo Seifert for valuable conversations, and V. Volpert and M. Schatzmann for acquainting us with Ref. [17]. J.B. was supported by an operating grant from the National Science and Engineering Research Council of Canada. L.S.T. was supported by a Chaire Louis Néel and by NSF Grants Nos. DMS-8910767 and DMS-9113142.

APPENDIX: NUMERICAL METHODS

To solve Eqs. (7) with boundary conditions (8) numerically, we discretize the real line $-\infty < x < \infty$ via a tanh mapping

$$x_n \equiv X \operatorname{arctanh}(2n/N), \quad n = -N/2, \ldots, N/2 . \tag{A1}$$

Grid points $x_{\pm N/2}$ are at $\pm\infty$, respectively, and the order parameters $p(x_{\pm N/2})$ and $q(x_{\pm N/2})$ are set equal to their boundary values (8). Grid points $x_{\pm(N/2-1)} = \pm X \operatorname{arctanh}(1-2/N)$ are the last finite points in the domain. The scale factor X is set to some multiple—usually 10—of the width w of the solution, i.e., the portion of the real line over which p and q vary from their boundary values. We study mainly solutions with two fronts (the 20 solution), separated approximately by w, which diverges as a function of the control parameter h (e.g., Figs. 3 and 7). This imposes two distinct numerical requirements on the grid (A1): X must be sufficiently large to contain both fronts, and each front must be resolved by a sufficient number of points. For a fixed number $N+1$ of points, this leads to a maximum width w for solutions which can be represented on the grid (A1). (See Fig. 16.) Solutions with only one front, i.e., the 21 or 10 solutions, do not suffer from this constraint.

We represent the spatial derivatives d/dx and d^2/dx^2 by centered finite-difference formulas on the grid (A1). Equations (7) with boundary conditions (8) then constitute an indeterminate system of $2(N+1)$ equations in the $2(N+1)+1$ unknowns $\{q(x_n),p(x_n),v\}$. The translational invariance of (7) and (8) can be broken by imposing any condition which fixes the midpoint of the solution. We usually use

$$q(0) = \tfrac{1}{2}[q(\infty)+q(-\infty)] . \tag{A2}$$

For cases in which $p \neq 0$, we sometimes impose

$$\frac{dp}{dx}(0) = 0 , \tag{A3}$$

or, more generally, a linear combination of (A2) and (A3).

Because system (7), (8), and (A2) can have turning points and multiple solutions over some ranges of the control parameter h, the values $\{q(x_n),p(x_n),v\}$ cannot be considered to be functions of h, and must be calculated by numerical continuation (see, e.g. [42]). That is, we treat h as an additional unknown and progressively calculate a branch, or curve of solutions described by the $2(N+1)+2$ values $\{q(x_n),p(x_n),v,h\}$. An additional equation must now be appended to the enlarged system, as we shall now describe.

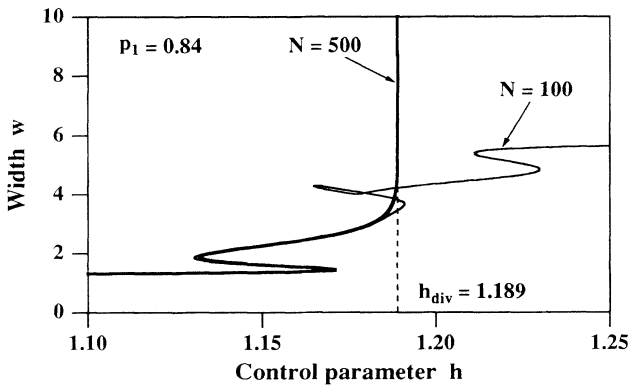

FIG. 16. Width of the 20 front vs h for 100- and 500-point resolution in x containing authentic $w \approx 2$ and spurious $w > 3$ saddle-node bifurcations. (Spurious bifurcations reflect insufficient resolution.)

We first compare the two most recent solutions and calculate which of $\{q(x_n),p(x_n),v,h\}$ has changed the most (weighing changes in h and v differently from the other variables). Let us call this distinguished continuation variable H, and predict the remaining components of the next solution point via linear or quadratic extrapolation in H. We then carry out Newton iteration to solve system (7), (8), and (A2), with the added condition that H retain its predicted value, i.e.,

$$H(\{q(x_n),p(x_n),v,h\}) = H_{\text{pred}} . \tag{A4}$$

Far from a saddle-node bifurcation the continuation variable is h. Near a saddle-node bifurcation h_{SN}, however, any other variable, e.g., v behaves like $|v_{\text{SN}}-v| \propto |h_{\text{SN}}-h|^{1/2}$. Hence, inevitably another variable will replace h as the continuation variable H as a saddle-node bifurcation is approached.

Each Newton iteration requires the solution of a linear system, setting the right-hand side equal to

$$J\Delta\{q(x_n),p(x_n),v,h\} , \tag{A5}$$

where J is the Jacobian of the combined system (7), (8), (A2), and (A4). The $2(N+1)\times 2(N+1)$ submatrix of J arising from (7) and (8) is septadiagonal. Extra rows result from the supplementary equations (A2) and (A4), and extra full columns result from the supplementary variables v and h. J can be factored into lower and upper triangular matrices in order to solve (A5) using time and storage proportional to N.

The only subtlety in forming J is the necessity for differentiating Eqs. (7), more specifically the free energy $F(q(x_n),p(x_n))$, with respect to h. F depends on h not only explicitly, but also implicitly via the nominal positions $(\hat{q}_j,\hat{p}_j)$. Thus the last column of J contains entries of the form

$$\frac{\partial F}{\partial h} + \sum_{j=0}^{2} \left[\frac{\partial F}{\partial \hat{q}_j}\frac{\partial \hat{q}_j}{\partial h} + \frac{\partial F}{\partial \hat{p}_j}\frac{\partial \hat{p}_j}{\partial h} \right] . \tag{A6}$$

Fortunately, the quantities $\partial\hat{q}_j/\partial h, \partial\hat{p}_j/\partial h$ are computed as byproducts of the Newton iteration for the nominal positions (2), while the other partial derivatives in (A6) are easily evaluated from (1) and (3)

The solution profiles used to initiate continuation at low values of h are smooth tanh-like interpolation between the boundary values, i.e., for q,

$$q(x) = q(\infty) + \frac{1(-\infty)-q(\infty)}{1+e^{10x}} . \tag{A7}$$

Information acquired as we proceed along the branch is used to calculate the next solution. As is standard, ΔH is set to be inversely proportional to the number of Newton iterations required to solve for the previous solution. As each new solution is calculated, its width is used to determine a new X. A new grid is calculated, and the solution

interpolated onto that grid, along with the two previous solutions.

Figure 16 illustrates the behavior of the finite-resolution continuation algorithm as the width of the solution diverges. The width w calculated using $N=100$ points agrees with that calculated using 500 points when $w<3$. For larger widths, the two curves diverge wildly. The insufficient resolution of the $N=100$-point curve is revealed by the spurious saddle-node bifurcations at high widths. (Such a phenomenon is also observed, for example, in a contour-dynamics simulation of vortex patches, where an increasing number of points along a contour eventually fails to represent a cusp in the asymptotic solution [43].) These spurious bifurcations reflect only a breakdown in the representation of solutions to (7), (8), (A2), and (A4) on the finite grid (A1): like a polynomial, the discretized system of coupled algebraic equations must gain and lose roots in pairs via saddle-node or pitchfork bifurcations. The $N=500$ representation also eventually breaks down, at still higher widths. Figure 16 also shows a pair of authentic saddle-node bifurcations near $w=2$. These survive increased resolution and reflect saddle-node bifurcations undergone by the differential equation on the infinite real line.

In order to study diverging traveling front solutions like that depicted in Fig. 5, which are not stationary in any moving frame, we integrate the time-dependent equations (6) in an adaptively translating frame [44]. We seek to define a frame position $\phi(t)$, measured in the stationary frame, which is midway between the two fronts. Transforming $x \rightarrow x+\phi(t)$ requires adding to the Eqs. (6) extra terms $\phi_t q_x$ and $\phi_t p_x$. We calculate $\phi(t)$ at each time step by updating the integral of the average velocity of the two fronts in the stationary frame. We then use Crank-Nicolson time stepping to propagate the diffusive terms in (6), and Adams-Bashforth to propagate the remaining terms connected with the free energy and the moving frame.

[1] For a summary of work on growing diamond, see Herbert M. Strong and Robert H. Wentorf, Jr., Am. J. Phys. **59**, 1005 (1991). The article includes an equilibrium pressure-temperature phase diagram of carbon.

[2] John C. Angus, Yaxin Wang, and Mahendra Sunkara, Annu. Rev. Mater. Sci. **21**, 221 (1991).

[3] There are four phases of solid manganese that appear as the temperature is increased: they are denoted α, β, γ, and δ. At room temperature and pressure, the α phase is stable, but the β phase can easily be observed under identical conditions by quenching from a temperature at which it is the stable phase. Ambient-pressure phase diagrams of the elements may be extracted from M. Hansen, *Constitution of Binary Alloys* (McGraw-Hill, New York, 1958).

[4] J. W. Martin and R. D. Doherty, *Stability of Microstructure in Metallic Systems* (Cambridge University Press, Cambridge, England, 1976).

[5] Frederick Seitz, *The Physics of Metals* (McGraw-Hill, New York, 1943), pp. 210–229.

[6] Tables of metastable phases are collected in the review by T. R. Anantharaman and C. Suryanarayana, J. Mater. Sci. **6**, 1111 (1971). The original article describing rapid solidification by "splat cooling" from the melt is by P. Duwez, R. H. Willens, and W. Klement, J. Appl. Phys. **31**, 1136 (1960).

[7] W. J. Boettinger and J. H. Perepezko, in *Rapidly Solidified Crystalline Alloys,* edited by S. K. Das, B. H. Kear, and C. M. Adam (The Metallurgical Society of AIME, New York, 1985), p. 21.

[8] If the melt temperature T is well above the roughening transition T_R, the interface velocity $v \propto (T_0-T)$, where T_0 is the solid-liquid equilibrium temperature. For $T \ll T_R$, one finds $V \propto (T_0-T)^2$, in the presence of screw dislocations. More generally, for $T \lesssim T_R$, one finds $v \propto (T_0-T)^\beta$, where $1<\beta<2$. In any case, one sees that if the roughening temperature of a metastable phase differs considerably from that of the stable phase, there will be a crossover in the growth rates as the undercooling is increased. See K. A. Jackson, Mater. Sci. Eng. **65**, 7 (1984).

[9] J. Bechhoefer, H. Löwen, and L. S. Tuckerman, Phys. Rev. Lett. **67**, 1266 (1991).

[10] J. G. Dash, Contemp. Phys. **30**, 89 (1989).

[11] S. Dietrich, in *Phase Transitions and Critical Phenomena,* edited by C. Domb and J. L. Lebowitz (San Diego, Academic Press, 1988), Vol. 21, p. 1. This article describes both wetting transitions and surface melting.

[12] J. W. Cahn, J. Chem. Phys. **66**, 3667 (1977).

[13] J. S. Rowlinson and B. Widom, *Molecular Theory of Capillarity* (Clarendon, Oxford, 1982, reprinted 1989), pp. 225–232.

[14] P. G. de Gennes, Rev. Mod. Phys. **57**, 827 (1985).

[15] T. Meister and H. Müller-Krumbhaar, Phys. Rev. Lett. **51**, 1780 (1983); Z. Phys. Abt. B **55**, 111 (1984).

[16] E. A. Brener and D. E. Temkin, Dokl. Akad. Nauk SSSR **266**, 1135 (1982) [Sov. Phys. Dokl. **27**, 778 (1982)]; Kristallografiya **28**, 18 (1983) [Sov. Phys. Cryst. **28**, 7 (1983)]; **28**, 244 (1983) [**28**, 142 (1983)]; **33**, 561 (1988) [**33**, 330 (1988)].

[17] Paul C. Fife and J. B. McLeod, Arch. Rat. Mech. Anal. **65**, 335 (1977).

[18] E. Ben-Jacob, H. Brand, G. Dee. L. Kramer, and J. S. Langer, Physica D **14**, 348 (1985).

[19] W. van Saarloos, Phys. Rev. A **37**, 211 (1988).

[20] Rowlinson and Widom (Ref. [13], p. 219) credit John W. Cahn with the idea that multiple order parameters lead to the possibility that both nonwetting and wetting interfaces are possible between two phases in the presence of a third phase.

[21] H. Löwen, T. Beier, and H. Wagner, Z. Phys. B **79**, 109 (1990); Europhys. Lett. **9**, 791 (1989).

[22] Andrea C. Levi and Erio Tosatti, Surf. Sci. **189/190**, 641 (1987).

[23] Glenn C. Paquette, Phys. Rev. A **44**, 6577 (1991).

[24] B. A. Malomed, A. A. Nepomnyashchy, and M. I. Tribelsky, Phys. Rev. A **42**, 7244 (1990).

[25] P. C. Hohenberg and B. I. Halperin, Rev. Mod. Phys. **49**, 435 (1977).

[26] See. e.g., P. R. Harrowell and D. W. Oxtoby, J. Chem.

Phys. **86**, 2932 (1987). For interfaces in equilibrium ($v=0$), the mechanical analogy has been often discussed. See, e.g., Ref. [13].

[27] J. Guckenheimer and P. Holmes, *Nonlinear Oscillations, Dynamical Systems, and Bifurcations of Vector Fields* (Springer-Verlag, New York, 1983), pp. 354–356.

[28] In many real systems that show surface melting, long-range forces change the logarithmic divergence into a power-law divergence. Including long-range forces in our discussion would have a similar result. See, for example, P. G. de Gennes, J. Phys. (Paris) Lett. **42**, L-377 (1981).

[29] B. Widom, J. Chem. Phys. **68**, 3878 (1978).

[30] Compare J. S. Rowlinson and B. Widom, *Molecular Theory of Capillarity* (Ref. [13]), pp. 221–225.

[31] H. Löwen and R. Lipowsky, Phys. Rev. B **43**, 3507 (1991).

[32] Eberhard Bodenschatz, John R. de Bruyn, Guenter Ahlers, and David S. Cannell, Phys. Rev. Lett. **67**, 3078 (1991).

[33] See, for example, S. Douady, J. Fluid Mech. **221**, 383 (1990).

[34] P. Oswald, J. Bechhoefer, A. Libchaber, and F. Lequeux, Phys. Rev. A **36**, 5832 (1987).

[35] P. Ribière and P. Oswald, J. Phys. France **51**, 1703 (1990).

[36] P. Oswald, J. Bechhoefer, and A. Libchaber, Phys. Rev. Lett. **58**, 2318 (1987).

[37] John Bechhoefer, Ph.D. thesis, The University of Chicago, 1988, pp. 157–175.

[38] Barbara H. Arendt, Senior thesis project, The University of Chicago, 1990.

[39] John Bechhoefer (unpublished).

[40] David W. Oxtoby and Peter R. Harrowell, J. Chem. Phys. **96**, 3834 (1992).

[41] John W. Cahn. J. Am. Ceram. Soc. **52**, 118 (1969).

[42] Rüdiger Seydel, *From Equilibrium to Chaos: Practical Bifurcation and Stability Analysis* (Elsevier, New York, 1988).

[43] R. Van Buskirk and P. S. Marcus (unpublished).

[44] H. Löwen, J. Bechhoefer, and L. S. Tuckerman, Phys. Rev. A **45**, 2399 (1992).